

Gate-tunable anisotropic Josephson diode effect in topological Dirac semimetal Cd_3As_2 nanowires

Yan-Liang Hou,¹ An-Qi Wang,² Na Li,² Chun-Guang Chu,²
Alexander Brinkman,¹ Zhi-Min Liao,² and Chuan Li^{1,*}

¹*MESA+ Institute for Nanotechnology,
University of Twente, Enschede 7500 AE, The Netherlands*

²*State Key Laboratory for Mesoscopic Physics and
Frontiers Science Center for Nano-optoelectronics,
School of Physics, Peking University, Beijing 100871, China*

(Dated: March 11, 2026)

Abstract

The intrinsic Josephson diode effect (JDE) has recently attracted considerable attention due to its sensitivity to broken symmetries in Josephson junctions, offering a powerful probe for uncovering hidden symmetry-breaking mechanisms in materials. The presence of higher-harmonic components in the current-phase relation, together with spin-orbital coupling, makes topological materials ideal platforms to explore this effect. In this work, we present a systematic study of the JDE in type-I topological Dirac semimetal Cd_3As_2 nanowire-based Josephson junctions. We observe a pronounced gate-tunable and highly anisotropic diode response under different magnetic-field orientations. By developing a comprehensive phenomenological model, we capture the angular dependence of the diode effect and, through temperature-dependent measurements, disentangle the respective contributions from bulk and topological surface states. Notably, anomalies in the temperature dependence of the diode efficiency reveal the coexistence of multiple transport channels, highlighting the Josephson diode effect as a sensitive probe of hidden topological superconducting states.

I. INTRODUCTION

The Josephson diode effect (JDE), characterized by a nonreciprocal critical current $|I_c^+| \neq |I_c^-|$, represents a fundamental departure from conventional Josephson transport and enables dissipationless rectification in superconducting circuits. Unlike normal-state diode effects, the JDE is intrinsically phase coherent and therefore highly sensitive to broken symmetries and the microscopic structure of the current-phase relation (CPR). Recent experiments have demonstrated Josephson diode behavior in a broad range of material platforms, including super-lattice[1], Rashba semiconductors [2, 3], engineered van der Waals heterostructures [4-8], and type-II Dirac and Weyl semimetals [9, 10], sparking intense interest in both fundamental mechanisms and device-oriented applications (see also the review in Ref. [11]).

From a symmetry perspective, a dc Josephson diode effect requires the simultaneous breaking of time-reversal symmetry (TRS) and a spatial symmetry that relates forward and backward supercurrents. However, symmetry breaking alone is generally insufficient. As can be understood from the spectrum of Andreev bound states, a non-sinusoidal CPR

* Corresponding author: chuan.li@utwente.nl

containing higher harmonics is typically required to lift the equality between positive and negative critical currents [2, 9]. Microscopically, such CPR asymmetry may arise from finite-momentum Cooper pairing or from the formation of a ϕ_0 -junction, where a phase shift $0 < \phi_0 < \pi$ is induced in the CPR [12, 13]. When combined with higher-harmonic components, these mechanisms lead to unequal supercurrent amplitudes for the positive and negative branches of the Andreev bound states [9, 14–17].

The interplay between superconductivity and topology is particularly appealing in this context. First, topological states with spin–momentum locking can strongly enhance finite-momentum pairing in the presence of TRS breaking [15, 18, 19]. Second, proximity-induced superconductivity in topological materials can host Majorana zero modes (MZMs), which are key building blocks for topological quantum computation [20, 21]. Recent theoretical works further suggest that parity-protected MZMs can significantly enhance the Josephson diode effect [19, 22–25]. Topological Dirac and Weyl semimetals (DSM and WSM) share many surface-state characteristics with topological insulators while offering a three-dimensional platform to study topological Josephson effects [26–28].

To date, the Josephson diode effect in topological materials has been predominantly reported in type-II DSM and WSM [9, 10]. However, the typical large bulk carrier density in type-II DSM/WSMs limits electrostatic tunability and complicates the disentanglement of surface and bulk contributions. In contrast, Cd_3As_2 is a type-I Dirac semimetal with ultrahigh mobility and low intrinsic carrier density [29], making it an attractive platform for gate-tunable proximity devices and surface-dominated transport [27, 30, 31]. This enables controlled realization of the Josephson diode effect via external fields, spin textures, and electrostatic gating, and provides a unique opportunity to disentangle surface and bulk transport channels [26].

In this work, we report a highly gate-tunable JDE in Cd_3As_2 nanowire-based Josephson junctions. The diode efficiency reaches a maximum near the Dirac point and exhibits an anomalous enhancement at elevated temperatures around 1.2 K. Notably, the gate and temperature ranges where the JDE is maximized coincide with a transport regime dominated by topological surface states, indicating a strong surface-mediated contribution to the JDE. In addition to large and tunable diode efficiencies, we observe a gate-dependent sign reversal of the diode effect and a pronounced anisotropy with respect to the in-plane magnetic-field orientation. We develop a phenomenological microscopic model incorporating finite-

momentum pairing, multi-harmonic CPR components, and interference between surface and bulk channels, which reproduces the main experimental observations and captures the gate and angular dependences of the JDE [17, 19, 23, 32].

II. RESULTS

In this work, we present measurements of three different devices, with nanowire diameters all about 100 nm and junction lengths between 400 nm and 800 nm. Unless otherwise specified, all data were acquired at a base temperature of 20 mK. A schematic of the device and the magnetic field orientations are shown in Fig. 1a.

A. Josephson diode effect in topological Dirac semimetal

Fig.1b shows the I_b - V characteristics at $V_g = 10$ V and $B_y = 10$ mT for up-sweeps (red) and down-sweeps (blue, solid line). While taking the absolute value of the negative current (blue dashed line), a clear asymmetry is observed between the critical currents I_c^+ and $|I_c^-|$, corresponding to the switching currents in the two sweep directions. If bias current amplitude is set between I_c^+ and $|I_c^-|$, the system remains superconducting in one current direction but becomes dissipative in the opposite direction, evidencing a rectification effect, so-called Josephson diode effect.

Fig. 1c shows the critical current I_c^+ (red) and $|I_c^-|$ (blue) as a function of the in-plane perpendicular magnetic field B_\perp^{in} at $V_g = 10$ V. At $B_\perp^{in} = 0$, $I_c^+ = |I_c^-|$, indicating the preserved TRS. It is clear to see that at the negative field, $|I_c^-|$ is larger than I_c^+ , and at the positive field, this is reversed, obeying an anti-symmetric dependence of the applied magnetic field.

This rectification effect is further illustrated in Fig. 1d, which shows the voltage response across the junction at $T = 20$ mK under selected in-plane magnetic fields $B_\perp^{in} = \pm 14, \pm 12, \pm 10, \text{ and } \pm 8$ mT. The blue curves denote the applied bias currents, while the red curves show the corresponding voltages across the junction. In all cases, the amplitude of the applied bias current lies between I_c^+ and $|I_c^-|$, leading to a pronounced rectification response. Moreover, the data reveal a reversal of the rectification polarity depending on the direction of the applied in-plane magnetic field.

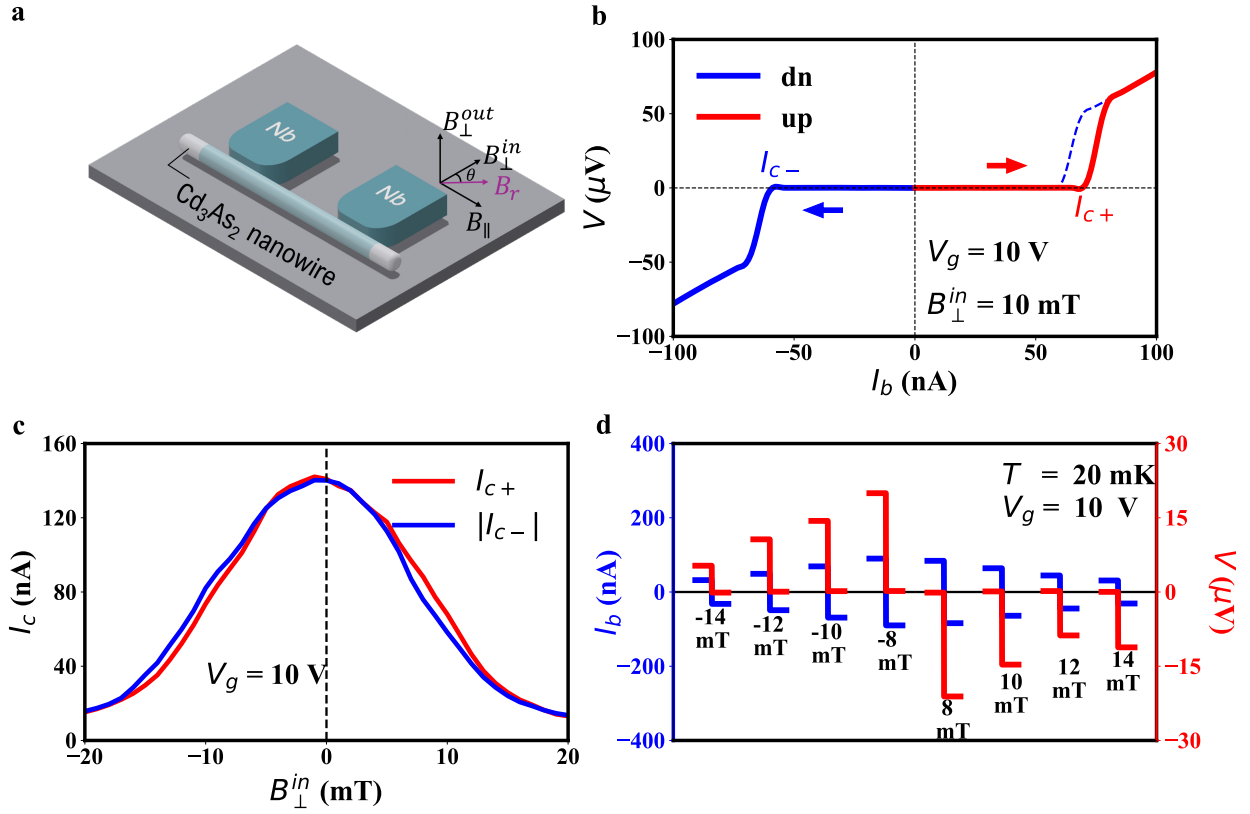


Fig. 1. **Josephson diode effect in Cd₃As₂ (device A: L=800 nm).** **a**, Schematic of an Nb–Cd₃As₂ nanowire–Nb Josephson junction. Magnetic field orientations are defined as in-plane perpendicular (B_{\perp}^{in}), in-plane parallel (B_{\parallel}), and out-of-plane (B_{\perp}^{out}); the angle θ is measured relative to B_{\perp}^{in} . **b**, I_b – V characteristics of up- and down-sweeps (starting from 0) at $V_g = 10$ V and $B_{\perp}^{in} = 10$ mT, showing pronounced nonreciprocal switching currents I_c^+ and I_c^- . Blue dotted curve: down-sweep data plotted in absolute value. **c**, Dependence of I_c^+ and $|I_c^-|$ on B_{\perp}^{in} at $V_g = 10$ V. **d**, Rectification effect at selected values of B_{\perp}^{in} .

B. Gate dependence

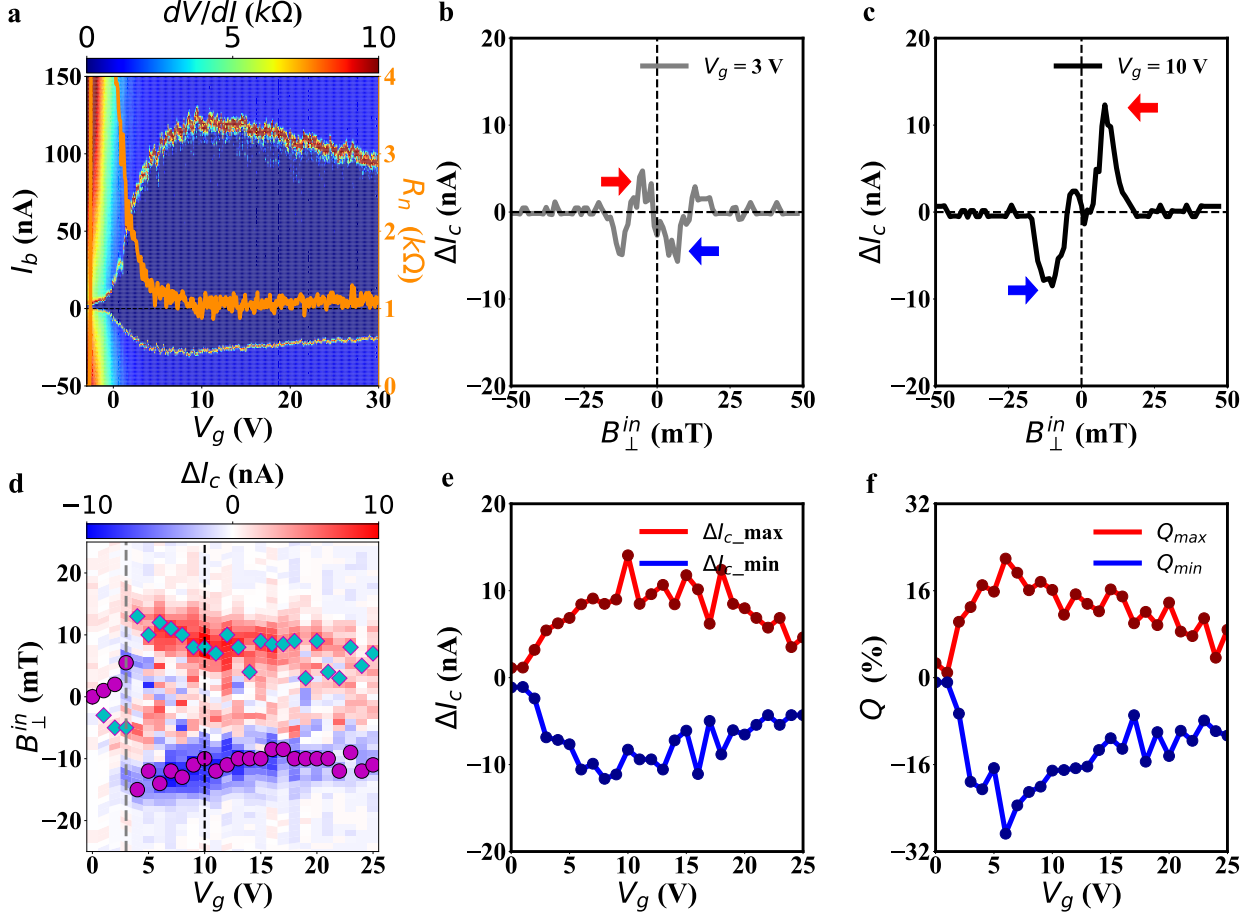


Fig. 2. **Gate dependence of the JDE (device A: $L=800$ nm).** (a) Differential resistance dV/dI as a function of gate voltage V_g and bias current I_b . The dark blue region corresponds to the superconducting state, which can be continuously tuned and eventually depleted by the gate. The orange curve on the right axis shows the normal-state resistance as a function of V_g . (b,c) Dependence of ΔI_c on the in-plane perpendicular magnetic field (B_{\perp}^{in}) at two representative gate voltages (3 V and 10 V). Blue and red arrows mark the minima and maxima of ΔI_c , respectively. (d) Colormap of ΔI_c as a function of V_g and B_{\perp}^{in} . Cyan and purple markers indicate the positions of the ΔI_c maxima and minima in B_{\perp}^{in} as a function of V_g . (e,f) Gate dependence of ΔI_c and of the Q-factor.

Applying a back-gate voltage strongly tunes the junction properties. In Fig. 2a, we show the dV/dI as function of bias current I_b and back-gate voltage V_g , where the dark-blue area indicates the superconducting regime. For positive gate voltages, the critical current

I_c increases rapidly and peaks near $V_g \approx 11$ V, after which it gradually decreases with further increasing V_g . For negative gate voltages, I_c is suppressed to zero within a few volts, indicating depletion of the supercurrent channel. Meanwhile, the normal-state resistance reaches a maximum and remains nearly constant over a wide negative range. A maximum in I_c near the Dirac point has been previously reported in similar systems [27, 30], attributed to an optimized surface-to-bulk contribution: as the Fermi level approaches the Dirac point, bulk carriers diminish more rapidly than topological surface carriers. As a result, the relative weight of surface transport is maximized near the Dirac point, giving rise to the observed maximum in I_c .

The JDE is characterized by the critical-current asymmetry $\Delta I_c \equiv I_c^+ - |I_c^-|$ and the efficiency factor $Q \equiv \frac{|\Delta I_c|}{(I_c^+ + |I_c^-|)/2}$. At each gate voltage, we apply an in-plane perpendicular field B_\perp^{in} , extract I_c^+ and $|I_c^-|$, and compute ΔI_c and Q . Figures 2b and 2c show $\Delta I_c(B_\perp^{in})$ at $V_g = 3$ V and 10 V. A finite diode signal appears at both polarities of the field. Two key features emerge: (1) the sign of ΔI_c reverses multiple times as the field increase; (2) the extrema of ΔI_c , denoted ΔI_c^{\max} and ΔI_c^{\min} (blue and red arrows), are tunable by the gate voltage V_g .

Previously, multiple sign changes in $\Delta I_c(B)$ were attributed to finite-momentum-induced phase modulation, $\sin(\pi B/B_d)$, where B_d is a characteristic field set by geometry and spin-orbit coupling (SOC) [33]. Smaller B_d produces more sign changes with field. However, the amplitude of ΔI_c should be bounded by the superconducting gap Δ_s , which usually follows $\Delta_s \propto [1 - (|B|/B_c)^2]^2$, implying a monotonic decrease in amplitude. This prediction contradicts our data, where the first lobe is smaller than the second. We attribute this unusual behavior to the coexistence of surface and bulk states. The amplitude of ΔI_c depends on many factors, including junction length, transport regime (ballistic or diffusive), and the resulting higher harmonics in the CPR [15]. Topological surface states, with spin-momentum locking, longer coherence lengths, and larger mean free paths [30], naturally yield a stronger JDE contribution. This suggests that the larger lobe in ΔI_c belongs to the surface states, which corresponds to $B_d^s \approx 15$ mT. The inner lobe corresponds to the bulk contribution, corresponding to a smaller $B_d^b \approx 5$ mT.

The gate tunability is further illustrated in Fig. 2d, where we plot ΔI_c as a function of both V_g and B_\perp^{in} . Figures 2b and 2c correspond to line cuts along the field axis at the gate voltages indicated by dashed lines in Fig. 2d. For each gate, we identify ΔI_c^{\max} and ΔI_c^{\min}

in $\Delta I_c(B)$ and trace their evolution in the 2D map using purple and black markers. The field position of the maximum ($B_{\perp,\max}^{\text{in}}$) varies with V_g . It remains nearly constant as V_g increases beyond the gate voltage that maximizes I_c ($V_g^{\text{max}} \sim 11$ V). In contrast, when V_g decreases below V_g^{max} , the corresponding $B_{\perp,\max}^{\text{in}}$ first increases, then rapidly drops to zero as the junction gets depleted. This suggests that while tuning the Fermi level, the properties of the states, e.g. effective SOC can be tuned, yielding a larger B_d .

The gate dependence of the $\Delta I_c^{\text{max}(min)}$ and the Q -factor are shown in Fig. 2e and 2f, respectively. Both quantities exhibit a pronounced maximum near 11 V and fall to zero at lower gate voltages. These distinctive trends are directly connected to the evolution of the topological surface states, further confirming that the observed JDE serves as a sensitive probe of topological transport channels.

C. Anisotropic angle dependence of the JDE

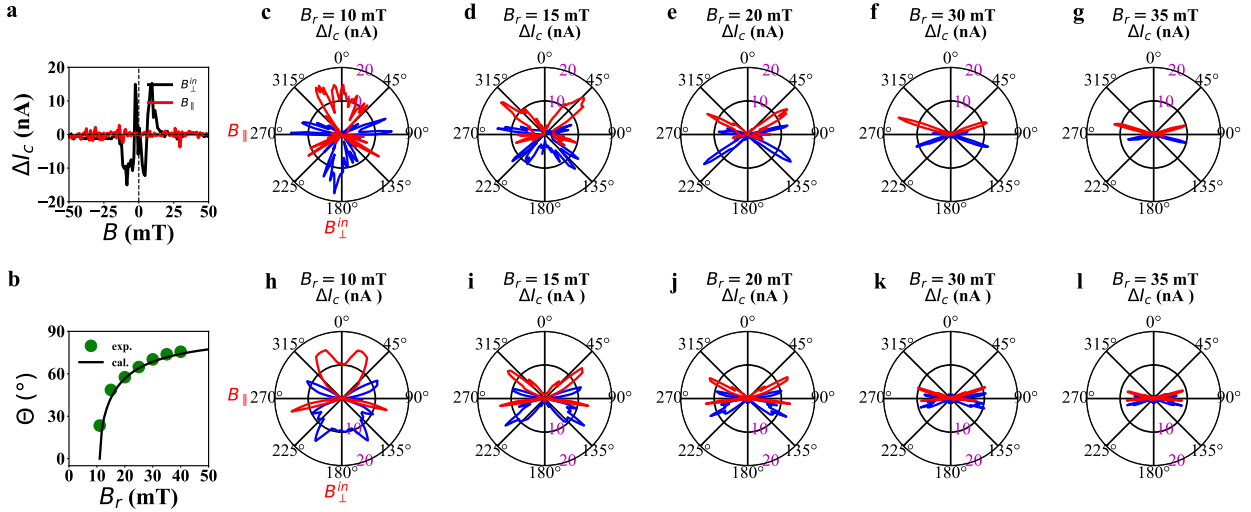


Fig. 3. In-plane angle dependence of the JDE (device B: $L=600$ nm). **(a)** ΔI_c as a function of B_{\perp}^{in} (black) and $B_{//}$ (red). **(b)** Angle corresponding to the maximum ΔI_c plotted against magnetic field strength B_r , comparing experimental data and theoretical calculations. **(c–g)** Experimental measurements of ΔI_c versus angle θ for different magnetic field strengths: $B_r = 10, 15, 20, 30,$ and 35 mT. The butterfly-shaped pattern of ΔI_c in polar coordinates becomes progressively compressed as B_r increases. **(h–l)** Calculated angular dependence of ΔI_c for the same set of magnetic field strengths.

To further investigate the observed JDE and the related symmetry-breaking, we rotate the magnetic field in different planes and measure its angle-dependence. First, we investigate the angle dependence in the plane same to the substrate. The experimental results for different field magnitude B_r are shown in Fig.3(c-g). In general, the JDE has a mirror symmetry and a two-fold rotation anti-symmetry. At small magnitude (e.g. $B_r=10\text{mT}$, Fig.3c), the ΔI_c is maximum along B_{\perp}^{in} (0°) direction. When the magnitude B_r is increased, the maximum ΔI_c is gradually rotated to the $B_{//}$ (90°) direction, and the lobes in the polar plot become more compressed. Therefore, the JDE becomes highly anisotropic at a higher magnitude of the field. In all cases, the JDE is anisotropic, and the principle axis of the anisotropy depends on the magnitude of the field.

This behavior mainly arises from the dominant contribution of the in-plane perpendicular field to the JDE. The overall response can be modeled as a linear combination of $\Delta I_c(B_{\perp}^{\text{ip}})$ and $\Delta I_c(B_{//})$. This distinction is clearly demonstrated in Fig. 3(a), where the ΔI_c values for both B_{\perp}^{ip} and $B_{//}$ are plotted on the same scale. Notably, the ΔI_c under a parallel field is practically negligible compared to that under the perpendicular field.

To qualitatively understand the angle dependence, we construct a ΔI_c polar plot based on the results in Fig. 3(a), by defining $\Delta I_c(\theta) = \Delta I_c(B_{\perp}^{\text{ip}}(\theta))$, where $B_{\perp}^{\text{ip}}(\theta)$ is obtained directly from the measurement as $B_{\perp}^{\text{ip}}(\theta) = B_r \cos \theta$. In Fig. 3(h-l), the calculated angular dependence at different magnitudes of B_r shows good agreement with the experimental results. For direct comparison, the angle corresponding to the maximum ΔI_c is plotted as a function of B_r in Fig. 3(b) for both experiment and calculation. The excellent agreement validates the linear combination model of the two field components in describing the JDE, which can also be extended to other angular planes.

An anisotropic JDE is also observed in the plane perpendicular to the wire. As shown in Fig. 4a, the critical supercurrent I_c decreases at different rates under applied magnetic fields in the out-of-plane (B_{\perp}^{out}) and in-plane (B_{\perp}^{in}) directions. Two notable observations can be made: First, contrary to the intuitive expectation that $I_c(B_{\perp}^{\text{out}})$ would decay faster than $I_c(B_{\perp}^{\text{in}})$ due to magnetic focusing, $I_c(B_{\perp}^{\text{in}})$ exhibits a more rapid decrease up to approximately 15 mT, followed by a slower decay toward the critical field. Second, both ΔI_c and the Q -factor oscillate around zero in both directions (Fig.4b and c). Such oscillating behavior can also be seen in the angle dependence at different field strengths (Fig.4 d). Given the wire's nearly square cross-section, we attribute these features to anisotropic spin-orbit coupling or

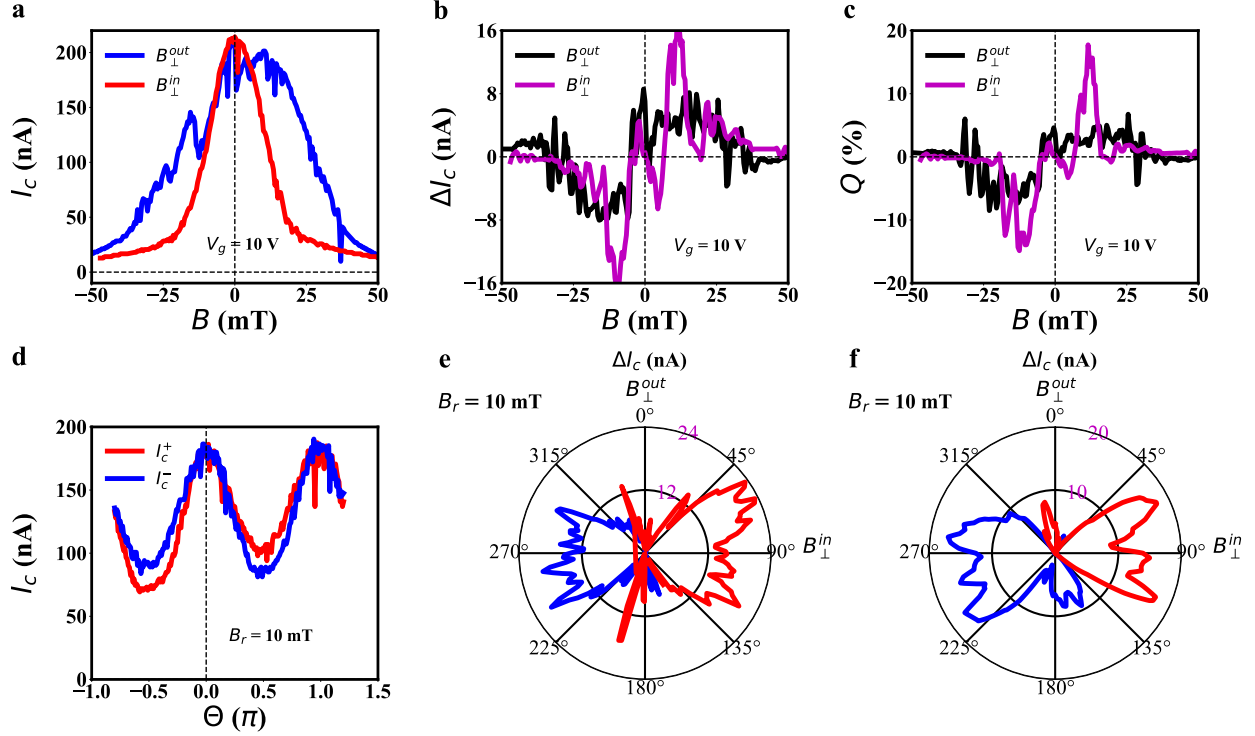


Fig. 4. **Angle dependence of the JDE in the plane normal to the wire (device C: $L=500$ nm).** (a) Magnetic-field dependence of the critical supercurrent I_c at $V_g = 10$ V. The value of I_c decreases under both in-plane perpendicular field B_{\perp}^{in} (red) and out-of-plane perpendicular field B_{\perp}^{out} (blue). (b,c) ΔI_c and the Q -factor as functions of magnetic field strength. (d) Angular dependence of I_c^+ and I_c^- at selected magnetic field strength ($B_r = 10$ mT). (e) Angular dependence of ΔI_c at selected magnetic field strength ($B_r = 10$ mT). (f) Calculated angular dependence of ΔI_c at selected magnetic field strength ($B_r = 10$ mT), using the results from (b).

an anisotropic g -factor in the material [34–36]. A quantitative determination of the SOC strength or the g -factor would require a dedicated experiment, which we leave for future work.

D. Temperature and length dependence

In the previous section, we demonstrated the gate-tunable JDE, with a pronounced enhancement arising from topological surface states. To further distinguish the JDE in the topological regime, we investigate its temperature dependence. Figure 5a shows the critical current as a function of the temperature $I_c(T)$ at $V_G = 10$ V. The I_c decreases rapidly with

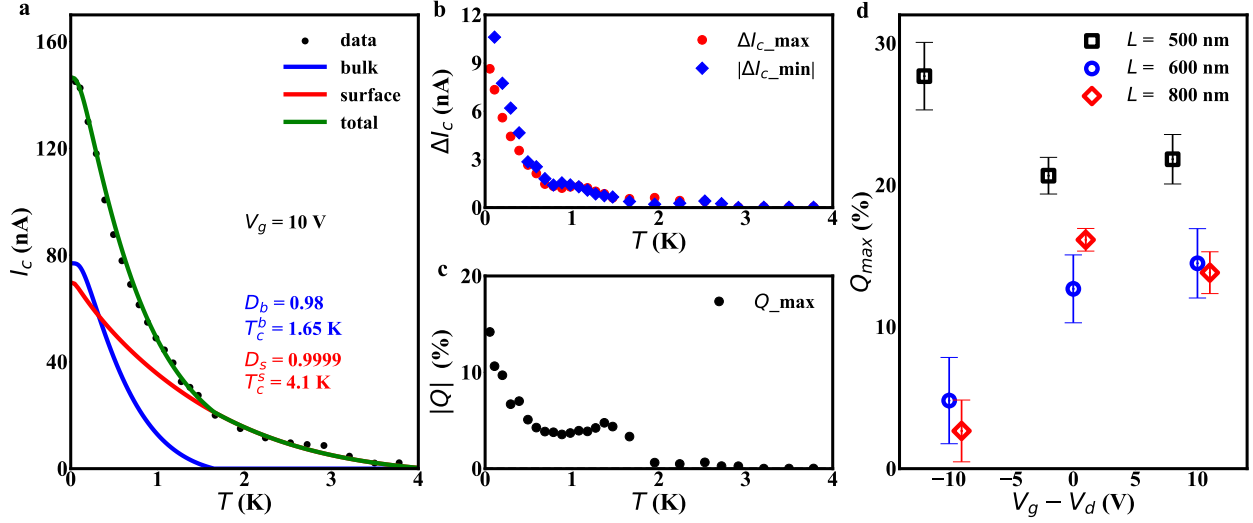


Fig. 5. **Temperature and length dependence of the JDE (device B: L=600 nm).** (a) Temperature dependence of I_c at $V_g = 10$ V. The measured I_c (black dots) decreases monotonically with increasing temperature. Two-channel Eilenberger fits are shown as solid lines for the surface contribution (red), bulk contribution (blue), and the total supercurrent (green). (b) Temperature dependence of ΔI_c corresponding to the maximal (red) and minimal (blue) values under positive and negative magnetic fields, respectively. (c) Temperature dependence of the Q -factor, revealing a pronounced enhancement near 1.3 K. (d) Gate dependence of the maximal Q -factor for junction lengths of 500, 600, and 800 nm.

temperature without saturation at low T . Given the long mean free path ($l_e \sim 600 - 1000$ nm) [30], this behavior is consistent with a ballistic junction regime. Around $T \sim 1.5$ K, a kink emerges in $I_c(T)$, suggesting a two-channel contribution. To capture this behavior, we fit the data using two-channel Eilenberger equations, assigning one channel to bulk states and the other to surface states.

The fitting parameters include the transparency D and the number of modes N (see SI for details). The superconducting coherence length is estimated as $\xi_s = \frac{\hbar v_F}{\pi \Delta^*}$, where v_F is the Fermi velocity, taken from literature [30], and Δ^* is the induced superconducting gap beneath the Nb electrodes, determined by the induced superconductivity T_c^* . We obtain $\xi_s^{\text{bulk}} \approx 300$ nm and $\xi_s^{\text{surf}} \approx 330$ nm (see supplementary material for the fitting parameters).

The fit reveals that the bulk channel (blue solid line in Fig. 5a) dominates for $T \lesssim 2$ K, but its contribution rapidly decreases with increasing temperature due to its ballistic nature.

In contrast, the surface channel persists to higher temperatures, consistent with topological protection, and produces the extended “tail” in $I_c(T)$, similar to previous observations in topological insulators [37].

Notably, near the crossover temperature, we observe a pronounced enhancement in both ΔI_c and the Q -factor (Fig. 5b,c), with a clear peak around 1.3 K. This suggests that as surface states begin to dominate, they contribute more strongly to the JDE than bulk states, leading to increased ΔI_c and Q . Such enhancement may serve as a hallmark of topological contributions in a multichannel system.

At the end, we present the gate-dependent JDE for junctions with different lengths. In Fig. 5d, we plot the maximum Q -factor of three junctions (with $L = 500, 600,$ and 800 nm) as a function of relative gate voltage with respect to the Dirac point (V_D). We find that the shortest junction ($L = 500$ nm) exhibits an overall larger Q -factor and does not show a maximum near $V_g = 10$ V, whereas the 600 nm and 800 nm junctions display very similar gate dependence, both peaking close to the Dirac point. This behavior highlights the importance of higher-harmonic contributions in the JDE: in shorter junctions, higher harmonics can participate more effectively, thereby enhancing the observed diode effect. The fact that the maximum is not present at the same gate voltage may be due to a higher electron-doping level in the junction when the length is short.

III. CONCLUSION

In conclusion, we demonstrate a gate-tunable Josephson diode effect in Cd_3As_2 -based Josephson junctions. By establishing a comprehensive model for the amplitude-dependent anisotropic JDE, we provide a clear framework for the rational design of devices with tailored diode anisotropy. Our results reveal a pronounced enhancement of the JDE in both its temperature and length dependence, highlighting the non-trivial interplay between topological surface states and bulk transport. These findings establish the Josephson diode effect as a powerful, symmetry-sensitive probe of topological states and pave the way toward novel superconducting devices and detection schemes based on topological quantum materials.

IV. METHOD

Material growth

The Cd_3As_2 nanowires were prepared by chemical vapour deposition method in tube furnace. Cd_3As_2 powders were placed at the centre of the furnace and silicon wafers coated with a thin gold film about 5 nm in thickness were used as substrates to collect the products downstream. First the tube furnace was flushed several times with Argon gas to fully remove oxygen. Then the temperature was gradually increased to 650 °C and kept for 10 min with an Argon flow of 20 s.c.c.m. as carrier gas. After the growth process, the furnace was cooled naturally.

Device fabrication

Cd_3As_2 nanowires were first transferred onto a substrate and patterned using standard electron-beam lithography. Subsequently, Nb/Pd (100/5 nm) contacts were deposited to serve as superconducting leads.

-
- [1] F. Ando, Y. Miyasaka, T. Li, J. Ishizuka, T. Arakawa, Y. Shiota, T. Moriyama, Y. Yanase, and T. Ono, Observation of superconducting diode effect, *Nature* **584**, 373 (2020).
 - [2] C. Baumgartner, L. Fuchs, A. Costa, S. Reinhardt, S. Gronin, G. C. Gardner, T. Lindemann, M. J. Manfra, P. E. Faria Junior, D. Kochan, J. Fabian, N. Paradiso, and C. Strunk, Supercurrent rectification and magnetochiral effects in symmetric Josephson junctions, *Nature Nanotechnology* **17**, 39 (2022).
 - [3] B. Turini, S. Salimian, M. Carrega, A. Iorio, E. Strambini, F. Giazotto, V. Zannier, L. Sorba, and S. Heun, Josephson diode effect in high-mobility insb nanoflags, *Nano Letters* **22**, 8502 (2022).
 - [4] H. Wu, Y. Wang, Y. Xu, P. K. Sivakumar, C. Pasco, U. Filippozzi, S. S. Parkin, Y. J. Zeng, T. McQueen, and M. N. Ali, The field-free josephson diode in a van der waals heterostructure, *Nature* **604**, 653 (2022).

- [5] L. Bauriedl, C. Bäuml, L. Fuchs, C. Baumgartner, N. Paulik, J. M. Bauer, K. Q. Lin, J. M. Lupton, T. Taniguchi, K. Watanabe, C. Strunk, and N. Paradiso, Supercurrent diode effect and magnetochiral anisotropy in few-layer nbse2, *Nature Communications* **13**, 4266 (2022).
- [6] F. K. de Vries, E. Portolés, G. Zheng, T. Taniguchi, K. Watanabe, T. Ihn, K. Ensslin, and P. Rickhaus, Gate-defined josephson junctions in magic-angle twisted bilayer graphene, *Nature Nanotechnology* **16**, 760 (2021).
- [7] J. Díez-Mérida, A. Díez-Carlón, S. Y. Yang, Y. M. Xie, X. J. Gao, J. Senior, K. Watanabe, T. Taniguchi, X. Lu, A. P. Higginbotham, K. T. Law, and D. K. Efetov, Symmetry-broken josephson junctions and superconducting diodes in magic-angle twisted bilayer graphene, *Nature Communications* 2023 14:1 **14**, 2396 (2023).
- [8] J. X. Lin, P. Siriviboon, H. D. Scammell, S. Liu, D. Rhodes, K. Watanabe, T. Taniguchi, J. Hone, M. S. Scheurer, and J. I. Li, Zero-field superconducting diode effect in small-twist-angle trilayer graphene, *Nature Physics* **18**, 1221 (2022).
- [9] B. Pal, A. Chakraborty, P. K. Sivakumar, M. Davydova, A. K. Gopi, A. K. Pandeya, J. A. Krieger, Y. Zhang, M. Date, S. Ju, N. Yuan, N. B. Schröter, L. Fu, and S. S. Parkin, Josephson diode effect from cooper pair momentum in a topological semimetal, *Nature Physics* **18**, 1228 (2022).
- [10] P. Chen, G. Wang, B. Ye, J. Wang, L. Zhou, Z. Tang, L. Wang, J. Wang, W. Zhang, J. Mei, W. Chen, and H. He, Edelstein effect induced superconducting diode effect in inversion symmetry breaking mote2 josephson junctions, *Advanced Functional Materials* **34**, 2311229 (2024).
- [11] M. Nadeem, M. S. Fuhrer, and X. Wang, The superconducting diode effect, *Nature Reviews Physics* **5**, 558 (2023).
- [12] F. Dolcini, M. Houzet, and J. S. Meyer, Topological josephson ϕ_0 junctions, *Phys. Rev. B* **92**, 035428 (2015).
- [13] T. Yokoyama, M. Eto, and Y. V. Nazarov, Anomalous josephson effect induced by spin-orbit interaction and zeeman effect in semiconductor nanowires, *Physical Review B - Condensed Matter and Materials Physics* **89**, 10.1103/PhysRevB.89.195407 (2014).
- [14] M. Davydova, S. Prembabu, and L. Fu, Universal josephson diode effect, *Science Advances* **8**, 309 (2022).
- [15] B. Lu, S. Ikegaya, P. Burset, Y. Tanaka, and N. Nagaosa, Tunable josephson diode effect on the surface of topological insulators, *Physical Review Letters* **131**, 096001 (2023).

- [16] A. Zazunov, J. Rech, T. Jonckheere, B. Grémaud, T. Martin, and R. Egger, Nonreciprocal charge transport and subharmonic structure in voltage-biased josephson diodes, *Physical Review B* **109**, 10.1103/PhysRevB.109.024504 (2024).
- [17] Y. Zhang, Y. Gu, P. Li, J. Hu, and K. Jiang, General theory of josephson diodes, *Physical Review X* **12**, 041013 (2022).
- [18] Y. Tanaka, B. Lu, and N. Nagaosa, Theory of giant diode effect in d -wave superconductor junctions on the surface of a topological insulator, *Physical Review B* **106**, 1 (2022).
- [19] J. Cayao, N. Nagaosa, and Y. Tanaka, Enhancing the josephson diode effect with majorana bound states, *Phys. Rev. B* **109**, L081405 (2024).
- [20] L. Fu and C. L. Kane, Superconducting proximity effect and majorana fermions at the surface of a topological insulator, *Phys. Rev. Lett.* **100**, 096407 (2008).
- [21] J. Linder, Y. Tanaka, T. Yokoyama, A. Sudbø, and N. Nagaosa, Unconventional superconductivity on a topological insulator, *Phys. Rev. Lett.* **104**, 067001 (2010).
- [22] H. F. Legg, K. Laubscher, D. Loss, and J. Klinovaja, Parity-protected superconducting diode effect in topological josephson junctions, *Physical Review B* **108**, 1 (2023).
- [23] S. Mondal, P.-H. Fu, and J. Cayao, Josephson diode effect with andreev and majorana bound states, arXiv preprint arXiv:2503.08318 (2025), submitted for publication.
- [24] J. Wang, Y. Jiang, J. J. Wang, and J.-F. Liu, Efficient josephson diode effect on a two-dimensional topological insulator with asymmetric magnetization, *Phys. Rev. B* **109**, 075412 (2024).
- [25] T. de Picoli, Z. Blood, Y. Lyanda-Geller, and J. I. Väyrynen, Superconducting diode effect in quasi-one-dimensional systems, *Phys. Rev. B* **107**, 224518 (2023).
- [26] I. Crassee and N. P. Armitage, 3d dirac semimetals: a review of material properties, *Physical Review Materials* **2**, 120302 (2018), review article.
- [27] C. Z. Li, A. Q. Wang, C. Li, W. Z. Zheng, A. Brinkman, D. P. Yu, and Z. M. Liao, Topological Transition of Superconductivity in Dirac Semimetal Nanowire Josephson Junctions, *Physical Review Letters* **126**, 027001 (2021).
- [28] C. Z. Li, A. Q. Wang, C. Li, W. Z. Zheng, A. Brinkman, D. P. Yu, and Z. M. Liao, Fermi-arc supercurrent oscillations in Dirac semimetal Josephson junctions, *Nature Communications* **11**, 1 (2020).

- [29] M. N. Ali, Q. Gibson, S. Jeon, B. B. Zhou, A. Yazdani, and R. J. Cava, The crystal and electronic structures of cd_3as_2 , the three-dimensional electronic analogue of graphene, *Inorganic Chemistry* **53**, 4062 (2014).
- [30] C. Z. Li, C. Li, L. X. Wang, S. Wang, Z. M. Liao, A. Brinkman, and D. P. Yu, Bulk and surface states carried supercurrent in ballistic Nb-Dirac semimetal Cd_3As_2 nanowire-Nb junctions, *Physical Review B* **97**, 115446 (2018).
- [31] C. Li, Z. Jia, X. Li, J. Shi, Z. Liao, D. Yu, and X. Wu, Aharonov-bohm oscillations in dirac semimetal cd_3as_2 nanowires, *Nature Communications* **7**, 10769 (2016).
- [32] A. Daido, Y. Ikeda, and Y. Yanase, Intrinsic superconducting diode effect, *Physical Review Letters* **128**, 037001 (2022).
- [33] B. Pal, A. Chakraborty, P. K. Sivakumar, M. Davydova, A. K. Gopi, A. K. Pandeya, J. A. Krieger, Y. Zhang, M. Date, S. Ju, N. Yuan, N. B. M. Schröter, L. Fu, and S. S. P. Parkin, Josephson diode effect from cooper pair momentum in a topological semimetal, *Nature Physics* **18**, 277 (2022).
- [34] J. Cao, S. Liang, C. Zhang, Y. Liu, J. Huang, Z. Jin, Z. G. Chen, Z. Wang, Q. Wang, J. Zhao, S. Li, X. Dai, J. Zou, Z. Xia, L. Li, and F. Xiu, Landau level splitting in cd_3as_2 under high magnetic fields, *Nature Communications* 2015 6:1 **6**, 1 (2015).
- [35] Z. K. Liu, J. Jiang, B. Zhou, Z. J. Wang, Y. Zhang, H. M. Weng, D. Prabhakaran, S. K. Mo, H. Peng, P. Dudin, T. Kim, M. Hoesch, Z. Fang, X. Dai, Z. X. Shen, D. L. Feng, Z. Hussain, and Y. L. Chen, A stable three-dimensional topological dirac semimetal cd_3as_2 , *Nature Materials* **13**, 677 (2014).
- [36] S. Jeon, B. B. Zhou, A. Gyenis, B. E. Feldman, I. Kimchi, A. C. Potter, Q. D. Gibson, R. J. Cava, A. Vishwanath, and A. Yazdani, Landau quantization and quasiparticle interference in the three-dimensional dirac semimetal cd_3as_2 , *Nature Materials* 2014 13:9 **13**, 851 (2014).
- [37] D. Rosenbach, T. W. Schmitt, P. Schüffelgen, M. P. Stehno, C. Li, M. Schleenvoigt, A. R. Jalil, G. Mussler, E. Neumann, S. Trellenkamp, A. A. Golubov, A. Brinkman, D. Grützmacher, and T. Schäpers, Reappearance of first Shapiro step in narrow topological Josephson junctions, *Science Advances* **7**, 1 (2021).

Gate-tunable anisotropic Josephson diode effect in topological Dirac semimetal Cd_3As_2 nanowires - Supplementary Information

Yanliang Hou,[†] Anqi Wang,[‡] Zhimin Liao,[‡] Alexander Brinkman,[†] and Chuan
Li*,[†]

[†]*MESA+ Institute for Nanotechnology, University of Twente, Enschede 7500 AE, The
Netherlands*

[‡]*State Key Laboratory for Mesoscopic Physics and Frontiers Science Center for
Nano-optoelectronics, School of Physics, Peking University, 100871 Beijing, China*

E-mail: Correspondingauthor:chuan.li@utwente.nl

Table 1: Parameters for two-channel Eilenberger fit

State	T_c (K)	ξ (nm)	Δ^* (μeV)	v_F (m/s)	R_n (Ω)	N (channels)
Bulk states	1.65	300	250.4	3.58×10^5	890	15
Surface states	4.10	330	622.3	9.79×10^5	3600	4

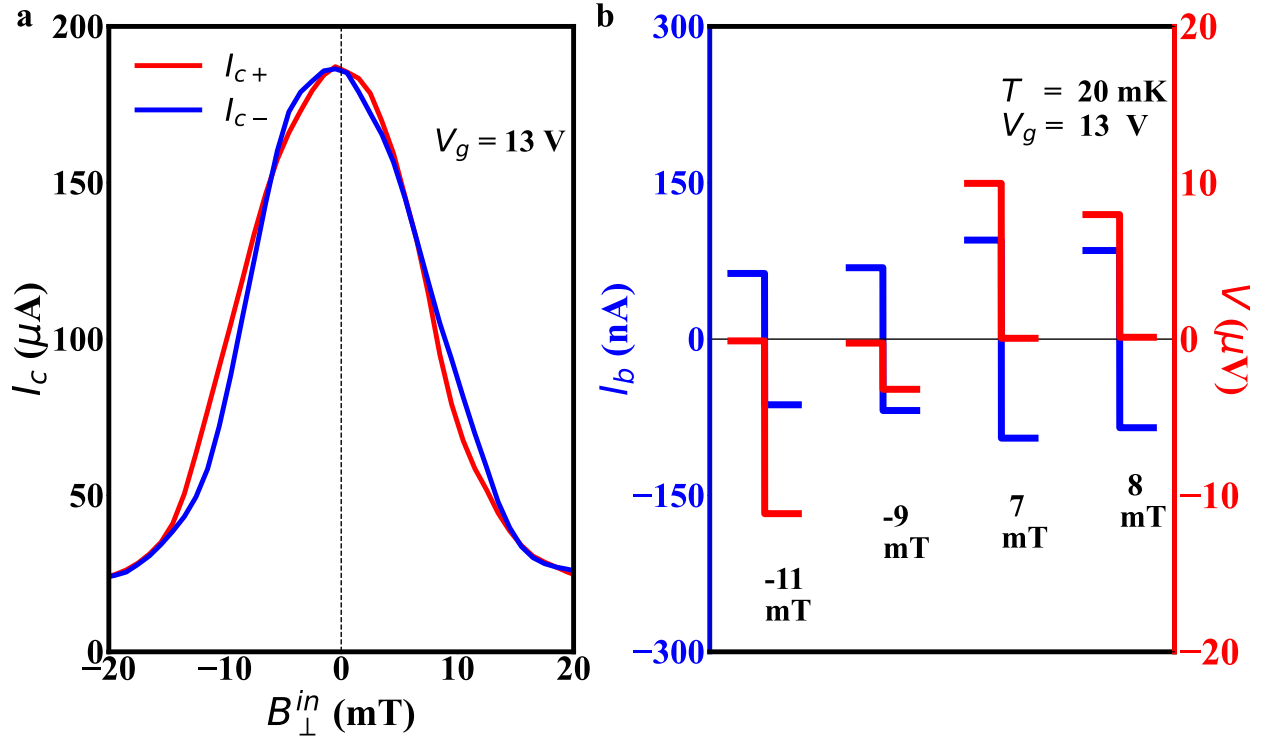


Figure S1: Josephson diode effect at 20 mK(device B: L=600 nm). (a) The switching supercurrent I_c^+ and $|I_c^-|$ as a function of B_{\perp}^{in} at $V_g=13$ V. It shows a largest asymmetry in switching supercurrent at $B_{\perp}^{in} \sim \pm 11$ mT.(b) Observed rectification effect in voltage across junction by using absolute value of bias current between I_c^+ and I_c^- at $T=20$ mK and under several selected values of B_{\perp}^{in} .

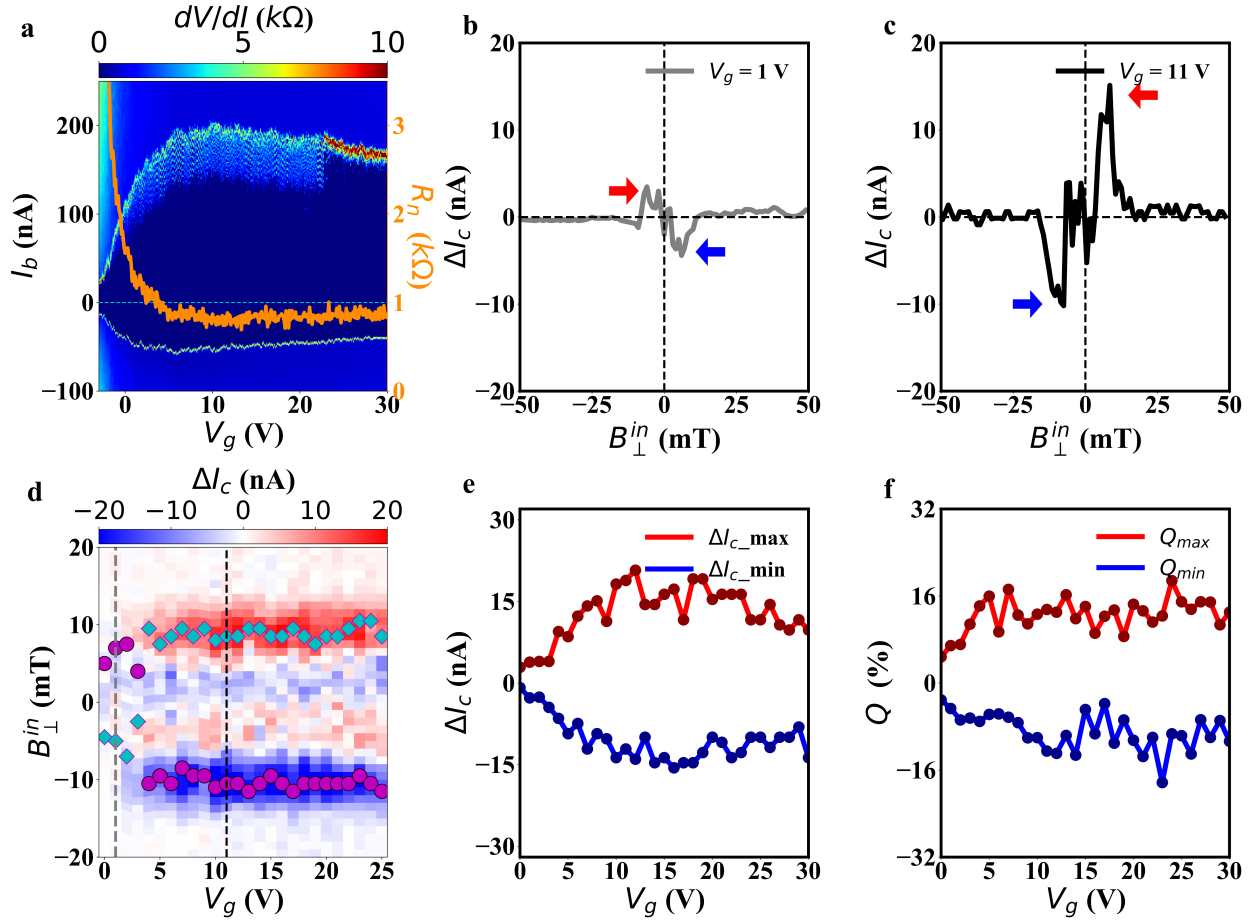


Figure S2: Gate voltage dependence of the Josephson diode effect at 20 mK (device B: L=600 nm). (a) Differential Resistance dV/dI as a function of applied gate voltage V_g and bias current I_b . It indicates that the critical supercurrent can be largely suppressed by the negative gate voltage. (b,c) Dependence of ΔI_c on in-plane perpendicular magnetic field B_{\perp}^{in} under $V_g=1$ V and $V_g=11$ V, respectively. Arrow in red shows the position of the curve's maximum point, while the arrow in blue indicates the position of the curve's minimum point. (d) ΔI_c as a function of applied gate voltage and in-plane perpendicular magnetic field. Diamond-shaped points in cyan mark the position of maximum value, while circular dot mark the position of minimum value. (e,f) ΔI_{c_max} , ΔI_{c_min} , Q_{max} , and Q_{min} as a function of V_g .

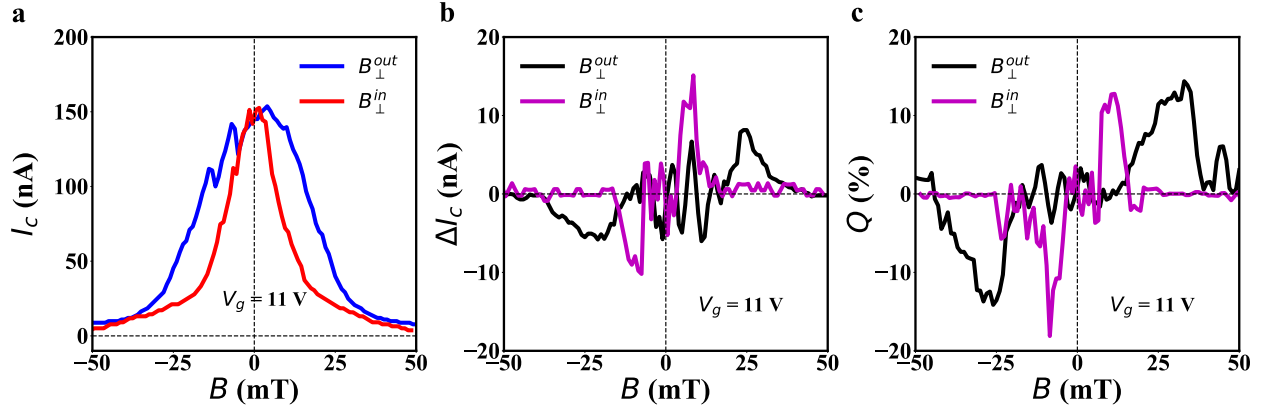
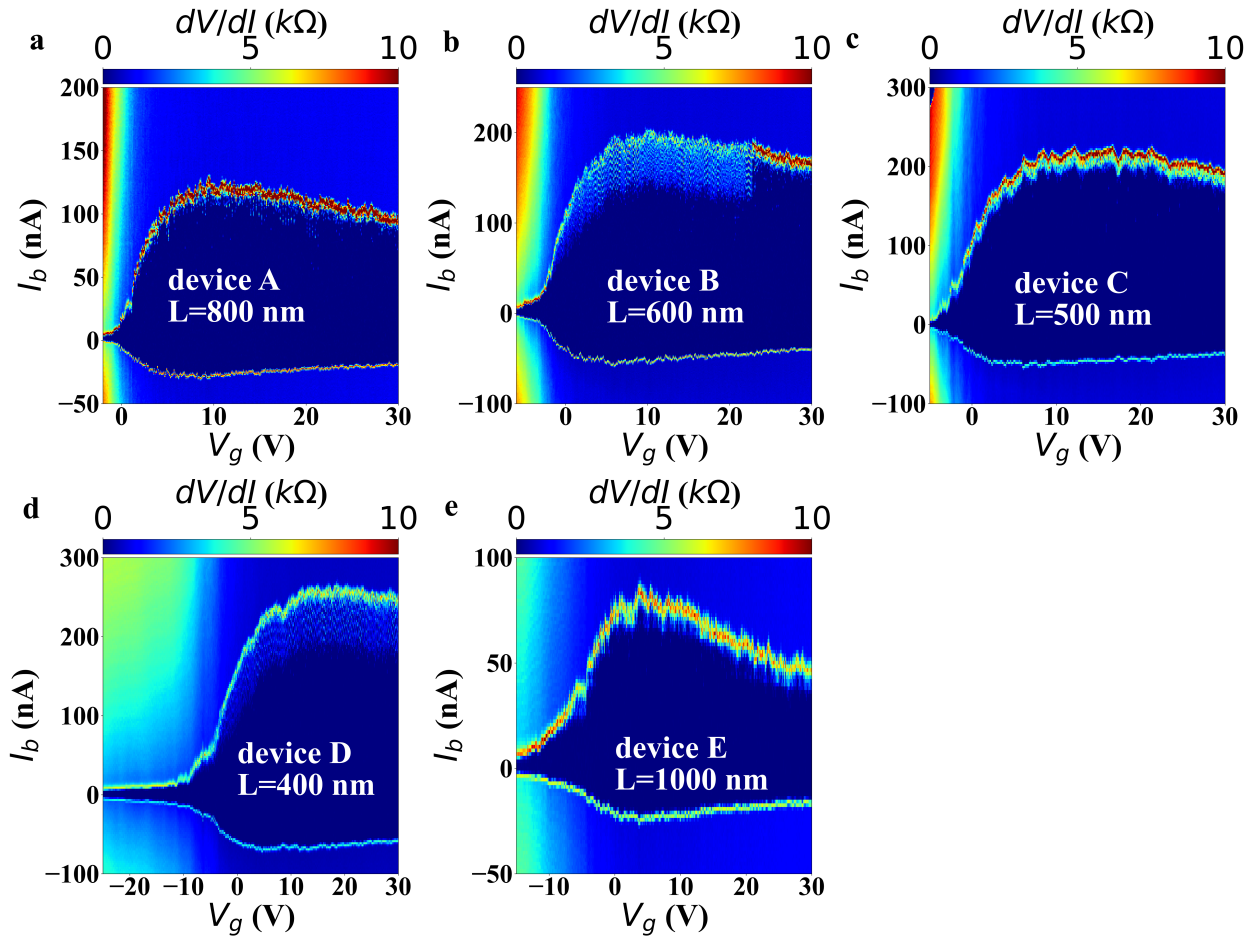
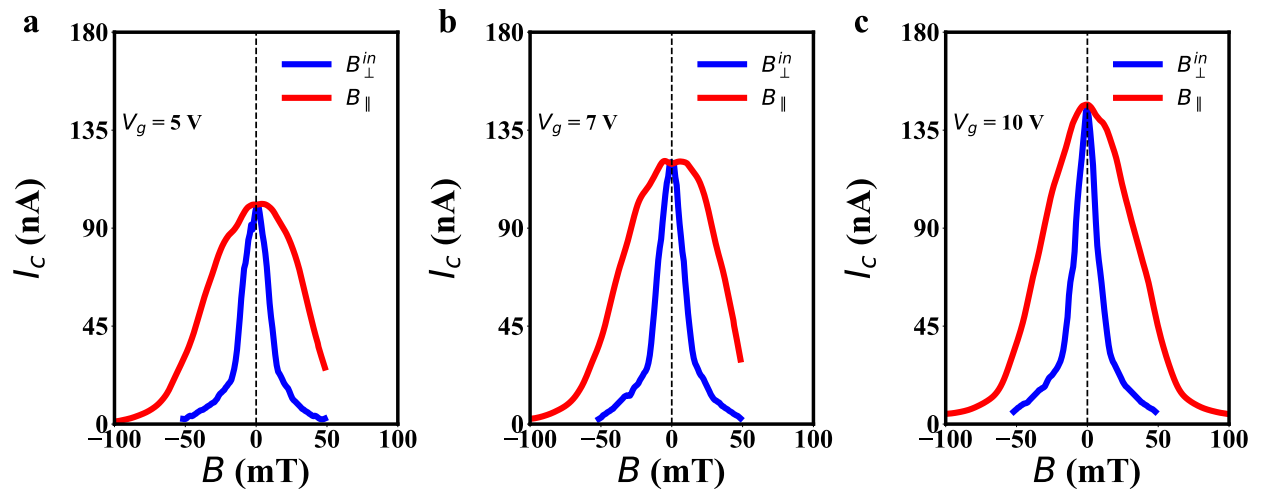


Figure S3: Angle-dependence of JDE in the plane that is perpendicular to the wire (device B: $L=600$ nm). (a) Dependence of critical supercurrent I_c on B_{\perp}^{out} and B_{\perp}^{in} , respectively. (b) ΔI_c as a function of B_{\perp}^{out} and B_{\perp}^{in} . (c) Q as a function of B_{\perp}^{out} and B_{\perp}^{in} .



SI-Fig S4: (a-e) Differential Resistance dV/dI as a function of applied gate voltage V_g and bias current I_b for device A-E. Length: $L=400$ nm, $L=500$ nm, $L=600$ nm, $L=800$ nm and $L=1000$ nm, respectively.



SI-Fig S5: (a-c) device B(L=600 nm) : Both I_c as a function of applied in-plane perpendicular magnetic field and I_c as a function of applied in-plane parallel magnetic field at $V_g=5$ V, 7V and 10V, respectively.